Journal of ELECTRONIC MATERIALS, Vol. 46, No. 7, 2017
DOI: 10.1007/s11664-017-5452-6

Structural, Elastic, Electronic and Optical Properties of LaOAgS-Type Silver Fluoride Chalcogenides: First-Principles Study

K. BOUDIAF,[1] A. BOUHEMADOU,[1,6] O. BOUDRIFA,[1] K. HADDADI,[1]
F. SAAD SAOUD,[2] R. KHENATA,[3] Y. AL-DOURI,[4] S. BIN-OMRAN,[5]
and M.A. GHEBOULI[1]

1.—Laboratory for Developing New Materials and Their Characterization, Department of Physics, Faculty of Science, University of Setif 1, 19000 Setif, Algeria. 2.—Department of Science and Technique, Faculty of Sciences and Technology, University of Bordj Bou-Arreridj, LMRN, 34000 Bordj Bou-Arreridj, Algeria. 3.—Laboratoire de Physique Quantique et de Modélisation Mathématique (LPQ3 M), Département de Technologie, Université de Mascara, 29000 Mascara, Algeria. 4.—Institute of Nano Electronic Engineering, Universiti Malaysia Perlis, 01000 Kangar, Perlis, Malaysia. 5.—Department of Physics and Astronomy, College of Science, King Saud University, P.O. Box 2455, Riyadh 11451, Saudi Arabia. 6.—e-mail: a_bouhemadou@yahoo.fr

First-principles density functional calculations were performed to investigate the structural parameters, elastic moduli and related properties, electronic band structure and optical properties of three LaOAgS-type barium silver fluoride chalcogenides BaAg*Ch*F (*Ch* denotes the chalcogenides S, Se and Te). The calculated structural parameters are in good accordance with the existing experimental data. The single-crystal and polycrystal elastic moduli were determined via the strain–stress technique. The investigated compounds show a strong anisotropic behaviour of the structural and elastic parameters. The calculated electronic band structure using the Tran–Blaha modified Becke–Johnson potential reveals that the three considered systems are large direct band gap semiconductors. The assignments of the energy band electronic states and chemical bonding character were accomplished with the help of the *l*-decomposed atomic densities of states diagrams. Frequency-dependent polarized optical functions were computed for an energy range from 0 eV to 30 eV. The microscopic origin of the electronic states that is responsible for the optical spectra structures were determined. The optical spectra exhibit a considerable anisotropy. Several trends in the variation of the considered physical properties with the atomic number Z of the chalcogenide *Ch* element in the BaAg*Ch*F series are observed.

Key words: 1111-like systems, first-principles calculations, elastic constants, electronic band structures, optical spectra

INTRODUCTION

The quaternary equiatomic LaOAgS-like systems, named also 1111 phases, form large family members (more than 200 compounds) in the crystal world.[1–8] This large class of quaternary materials exhibits some interesting physical properties, such as thermoelectricity,[6] transparency,[9] degenerate *p*-type electrical conductivity,[5] ferromagnetic response,[10] ionic conductivity[8] and medium-temperature superconductivity.[11,12] Owing to these outstanding physical properties, these 1111-like systems have various technological applications, such as *p*-type transparent semiconductors,[7,13] thermoelectrics,[14] optoelectronic devices[15] and photovoltaics.[16] The whole set of the 1111-like systems can be classified into two main

---

(Received November 26, 2016; accepted March 13, 2017;

subgroups.[3,12] The first one comprises metallic-like phases, which attract the attention of researchers for their superconductivity and magnetic properties.[11,17] The second one comprises the 1111-like systems exhibiting semiconducting behavior, which possess some interesting optical properties.[9,18–21] The 1111-like materials show a high flexibility to a large variety of constituent elements. The 1111-like oxychalcogenides have attracted the main attention of the researchers; however, much less investigations have been performed on the 1111-like chalcogenide fluorides.[12,21]

Recently, quaternary barium silver fluoride chalcogenides BaAg*Ch*F (*Ch* = S and Se) have been synthesized by Charkin et al.[2] via solid-state reactions of powdered Ba*Ch*, BaF_2 and Ag_2Ch (or Ba, BaF_2, Ag and *Ch*). Synthetic details, XRD characterisations and structural properties of the above-mentioned materials can be found in Ref. 2 These systems adopt the tetragonal $P4/nmm$ (No. 129) crystalline structure, $Z = 2$.[2] On the theoretical side, Bannikov et al.[12] calculated the electronic structures and optical spectra of BaAgSF and BaAgSeF employing the full-potential linearized augmented plane wave (FP-LAPW) method within the Perdew–Burke–Ernzerhof version of the generalized gradient approximation (GGA-PBE).[22] However, the GGA is well known by its misjudgment of the energy band gaps for semiconducting and insulating compounds. Typically, the energy band gap calculated through density functional theory (DFT) within the standard GGA/LDA is underestimated by approximately 30–50% compared to the measured one.[23–25] Accurate determination of the energy band dispersion and optical spectra of materials are especially required for eventual applications in the optoelectronic devices.[26] This constitutes the first objective of the present work. For technological applications in the optoelectronic field, the semiconductor materials are generally grown as thin films on substrates. However, the lattice mismatch and difference in thermal expansion coefficients between the epitaxial layer and substrate can produce large stresses in the grown layer.[27] Hence, it is of extreme importance to estimate the elastic moduli that describe the response of materials to external stresses. To the best knowledge of the authors, there is no available data in the literature on the elastic constants (C_{ij}s) of the studied BaAg*Ch*F crystals. Therefore, it becomes necessary and important to calculate the C_{ij}s of the BaAg*Ch*F compounds in order to disclose their elastic properties. Prediction of the elastic moduli and related properties of the BaAg*Ch*F series constitutes the second objective of the present work. A third objective of the present work is the investigation of the aforementioned properties for the hypothetical compound BaAgTeF, which is still completely unexplored to the best of our knowledge.

COMPUTATIONAL DETAILS

Two complementary codes based on the density functional theory were employed for a complete investigation of the structural parameters, elastic moduli, electronic properties and optical spectra of the barium silver fluoride chalcogenides BaAg*Ch*F (*Ch* = S, Se, Te).

The first part of the present work, namely, the structural optimization and elastic constants, was performed using the first-principles plane wave pseudopotential (PW-PP) approach as implemented in the CASTEP suite of programs.[28] The exchange–correlation functional was treated through the local density approximation (LDA)[29] and two different parameterizations of the GGA, namely, the GGA-PBE (termed also GGA96)[22] and the GGA-PBEsol (labelled also GGA08).[30] The GGA08 functional has been especially elaborated in order to improve the exchange–correlation potential modelling in solids. The Vanderbilt ultrasoft pseudopotentials[31] were used to model the interaction of the valence electrons with the nucleus and frozen core electrons. The electronic configurations for pseudo-atoms are Ba: $5s^2 5p^6 6s^2$, Ag: $3d^{10} 5s^1$, F: $2s^2 2p^5$, S: $3s^2 3p^4$, Se: $4s^2 4p^4$ and Te: $5s^2 5p^4$. A kinetic energy cut-off of 400 eV and a Monkhorst–Pack algorithm[32] with a $12 \times 12 \times 5$ *k*-point mesh to sample the Brillouin zone (BZ) were used to ensure a total energy convergence of 10^{-6} eV/atom. The following convergence criteria: total energy variation smaller than 5.0×10^{-6} eV/atom, maximum force on any atom smaller than 0.01 eV/Å^{-1}, stress smaller than 0.02 GPa and atomic displacement smaller than 5.0×10^{-4} Å were used to perform the full geometry optimization via the BFGS minimization algorithm.[33] The six single-crystal independent elastic constants, namely C_{11}, C_{33}, C_{44}, C_{66}, C_{12} and C_{13}, were determined by means of a linear fitting of the stress–strain data obtained from first-principles calculations.[28] The polycrystalline aggregate elastic moduli, namely the bulk (B) and shear (G), were derived from the single-crystal elastic constants via the Voigt–Reuss–Hill approach.[34]

Generally, the common GGA and LDA yield unsatisfactory band gap values compared to the corresponding measured ones for semiconductors and insulators. This is because the standard GGA/LDA cannot describe accurately the excited electronic states. Some functionals beyond the GGA/LDA are developed in order to improve the treatment of the exchange–correlation potential and consequently better describing the electronic structures of semiconductors and insulators. Among these functionals, which yield an improved band gap compared to the standard functionals, we find the Tran–Blaha modified Becke–Johnson (TB-mBJ) potential.[35–37] The TB-mBJ functional yields accurate fundamental band gap values for large families of semiconductors and isolators.[38] The predicted band gap values using the TB-mBJ are almost comparable with the experimental ones but with much less computing time compared to the sophisticated hybrid functionals and GW method. For this reason, the electronic and optical properties of the examined systems were studied using the TB-mBJ functional as implemented in the WIEN2k package[39] in order to provide electronic structure data more accurate than those reported previously.[12] The WIEN2k code[39] is an implementation of the full-potential linearized augmented plane wave (FP-LAPW) formalism based on the DFT. It is worth to note that the TB-mBJ potential functional is optimized to reproduce the energy band gaps of semiconducting and isolating materials and cannot be used for structural and elastic properties.[6] For the structural and elastic properties, we used the GGA-PBEsol, which is well tested for solids.[30]

The complex dielectric function: $\varepsilon(\omega) = \varepsilon_1(\omega) + i\varepsilon_2(\omega)$ characterizes the linear response of matter to incident radiation. The imaginary part $(\varepsilon_2(\omega))$ of the dielectric function $(\varepsilon(\omega))$ characterizes the absorption of the incident light by matter and can be computed by summing all allowed electronic transitions from occupied to unoccupied states. The real part $(\varepsilon_1(\omega))$ characterizes the dispersion of the incident radiation when it traverses a medium and can be derived from $\varepsilon_2(\omega)$ via the Kramer–Kronig transformation. The knowledge of both $\varepsilon_1(\omega)$ and $\varepsilon_2(\omega)$ permits one to compute all other macroscopic optical constants. To obtain accurate results for the optical constants, a dense *k*-point set is necessary. A $24 \times 24 \times 11$ *k*-point mesh was employed to calculate the dipole matrix element, which is the key for the optical spectra.

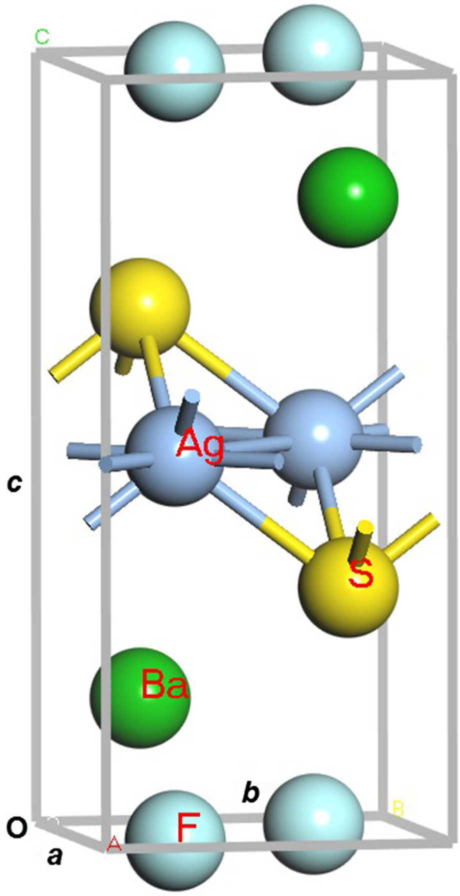

Fig. 1. The unit-cell crystalline structure of BaAgSF layered structure.

RESULTS AND DISCUSSION

Structural Properties

One conventional cell of the BaAgSF compound is depicted in Fig. 1 as a prototype for the BaAg*Ch*F series. As described elsewhere,[2] the barium silver fluoride chalcogenides BaAg*Ch*F (*Ch* = S, Se, Te) crystalize in a tetragonal layered structure of the LaOAgS-type with the space group *P4/nmm* and may be schematically viewed as an alternating stacking of quasi two-dimensional [BaF] and [Ag*Ch*] layers along the *c*-axis.[21] The Wyckoff positions of the four inequivalent atomic positions in the BaAg*Ch*F compounds are Ba: 2*c* (0.25, 0.25, z_{Ba}), Ag: 2*b* (0.75, 0.25, 0.5), *Ch*: 2*c* (0.25, 0.25, z_{Ch}) and F: 2*a* (0.75, 0.25, 0), where z_{Ba} and z_{Ch} are the internal *z*-coordinates of the Ba and chalcogen *Ch* atoms, respectively. The calculated equilibrium unit-cell parameters (*a* and *c*) and internal atomic coordinates (z_{Ba} and z_{Ch}) for each considered compound and the corresponding measured and previously calculated values (when available) are collected in Table I. Owing to the fact that the experiments were performed at room temperature whereas our results are predicted for zero temperature, one would expect that correct calculated values for the lattice parameters will be slightly smaller than their corresponding measured ones. From Table I, one can note that the GGA96-calculated (LDA-calculated) lattice parameters of the three considered compounds are somewhat larger (somewhat smaller) than the measured ones. This stems from the well-known fact that the LDA tends to slightly underestimate the interatomic distances, and the GGA96 tends to slightly overestimate them. However, from Table I, one can appreciate that the GGA08 calculated lattice parameters are practically equal to the arithmetic averages of the GGA96 and LDA-calculated values and are slightly smaller than their corresponding experimental ones, as expected. It is worth to note that the GGA08[30] has been developed specifically to improve the description of the exchange–correlation effects in solids. The maximum discrepancy between the GGA08-calculated structural parameters and the experiment is about 1.5% for the *c* parameter and less than 1% for the remaining parameters, which demonstrates the reliability of the obtained results. Therefore, the GGA08 optimized structural parameters were adopted for the calculations of the remaining investigated properties. The unit-cell parameters, *a* and *c*, increase when the chalcogenide atom *Ch* is substituted in the following sequence:

Table I. Calculated lattice parameters (a and c, in Å), internal atomic coordinates (z_{Ba} and z_{Ch} (Ch = S, Se and Te), dimensionless), unit-cell volume (V, in (Å^3)), cohesion energy (E_{coh}, in eV), formation enthalpy (ΔH, in eV) for the BaAg*Ch*F compounds, compared with available experimental and theoretical data

	BaAgSF			BaAgSeF			BaAgTeF
Property	This work	Expt.[A]	Other[B]	This work	Expt.[A]	Other[B]	This work
a	4.2047[a]	4.2406	4.280	4.2982[a]	4.3449	4.345	4.5015[a]
	4.1420[b]			4.2463[b]			4.4332[b]
	4.2785[c]			4.3679[c]			4.5018[c]
	4.2047[d]			4.3108[d]			4.5078[d]
c	9.1718[a]	9.3029	9.411	9.2690[a]	9.4018	9.558	9.5170[a]
	9.0004[b]			9.0849[b]			9.2666[b]
	9.3918[c]			9.5186[c]			9.5164[c]
	9.2365[d]			9.3203[d]			9.5024[d]
V	162.15[a]	167.29		171.24[a]	177.49		192.85[a]
z_{Ba}	0.1676[a]	0.1665		0.1616[a]	0.1598		0.1472[a]
	0.1693[d]			0.1624[d]			0.1494[d]
z_{Ch}	0.6743[a]	0.6760		0.6796[a]	0.6798		0.6859[a]
	0.6747[d]			0.6809[d]			0.6846[d]
E_{Coh}	−5.0056[a]			−4.8942[a]			−4.6850[a]
ΔH	−2.0536[a]			−2.4271[a]			−1.9476[a]

[a]Present, using GGA08 (PP-PW).[b]Present, using LDA.[c]Present, using GGA-PBE.[d]Present, using GGA08 (FP-LAPW).[A]Ref. 2.[B]Ref. 11.

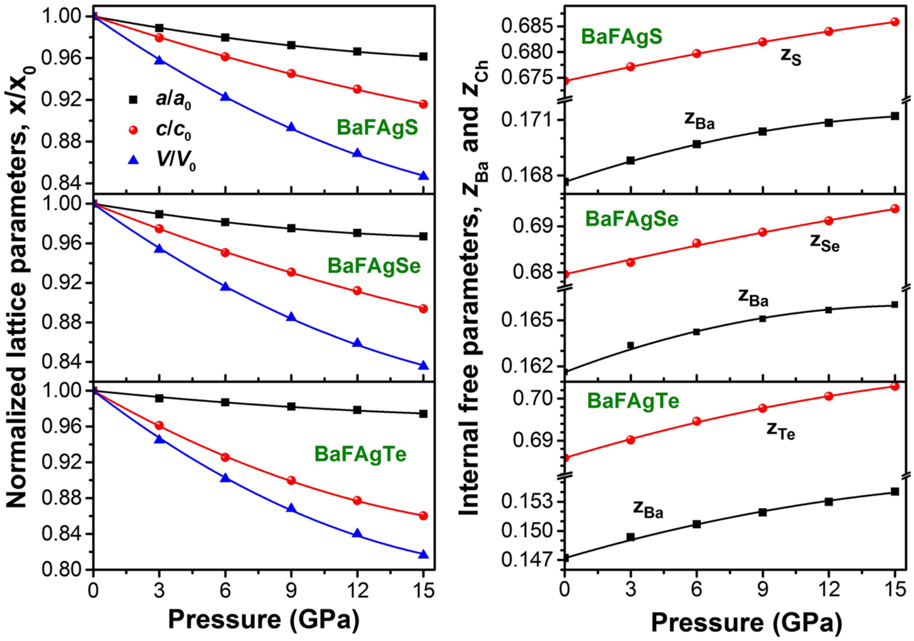

Fig. 2. Pressure dependence of the lattice parameters (a and c) and internal coordinates (Z_{Ba} and Z_{Ch}) for BaAgSF, BaAgSeF and BaAgTeF.

S → Se → Te in the BaAg*Ch*F series. This is a consequence of the increase of the *Ch* atomic radii (R); $R(S) = 1.09$ Å $< R(Se) = 1.22$ Å $< R(Te) = 1.42$ Å. One can appreciate that the calculated cohesive energy and formation energy (see Table I) are negative for each investigated compound, indicating that all studied compounds (including the hypothetical one; BaFAgTe) are chemically stable, confirming the fact that these compounds can be easily synthesized.

Pressure dependence of the relative shrinkage of the lattice parameters (a/a_0 and c/c_0) and unit-cell volume (V/V_0) and the internal atomic coordinates (z_{Ba} and z_{Ch}) are visualized in Fig. 2 (V, a, c, z_{Ba} and z_{Ch} are the values of the corresponding parameters at a fixed pressure P, whereas V_0, a_0 and c_0 are the corresponding values at zero pressure). In Fig. 2, the symbols represent the calculated results and solid lines represent the fits of these results to a second-order polynomial. One can appreciate that the

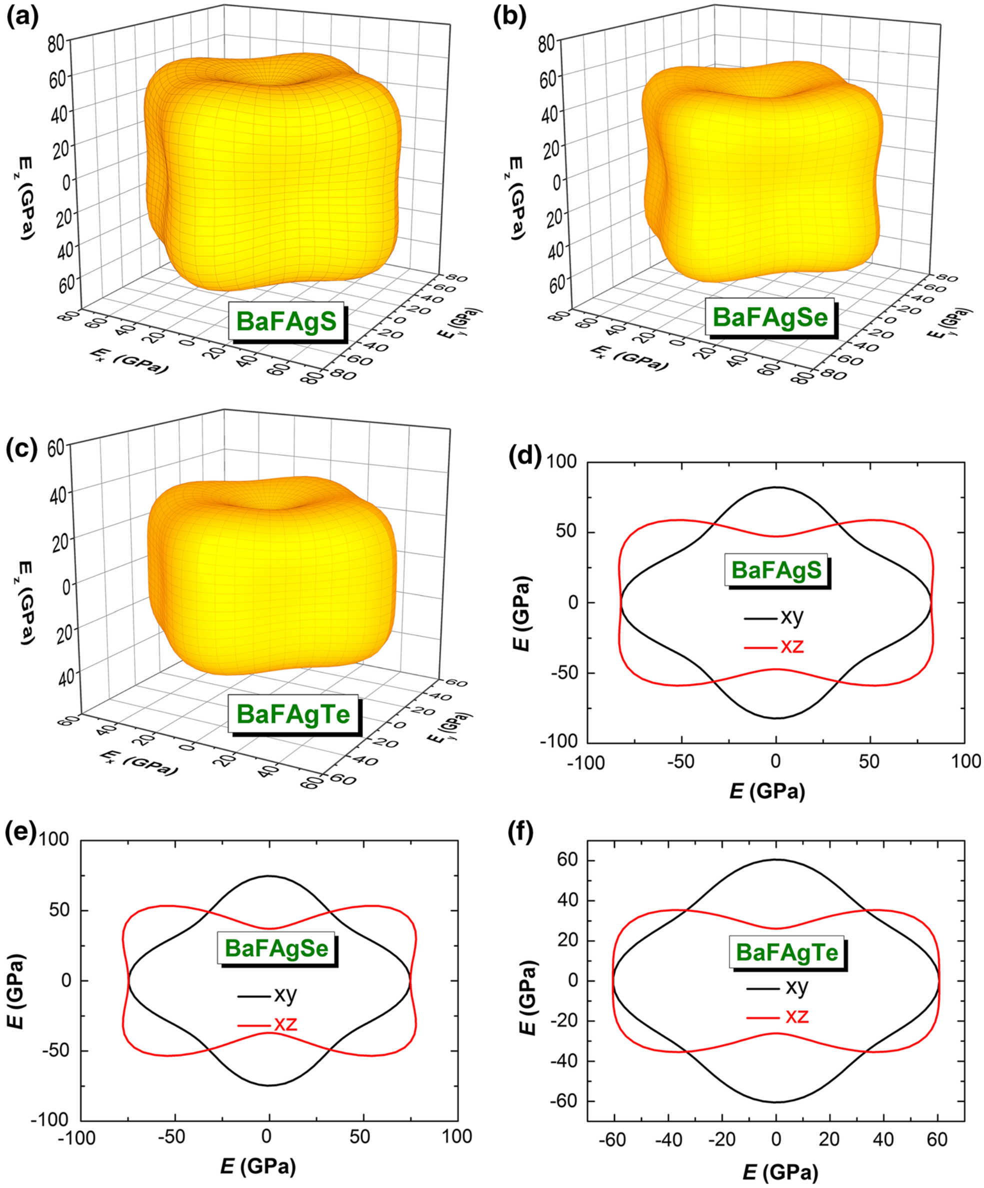

Fig. 3. The Young's modulus 3-D-representation for BaAgSF (a), BaAgSeF (b) and BaAgTeF (c) and their cross-section in the *xy* and *xz* planes (BaAgSF (d), BaAgSeF (e) and BaAgTeF (f)).

shrinkage along the c-axis is faster than that along the a-axis, indicating that the chemical bonding between the blocks [Ag*Ch*] and [BaF] along the c-axis are weaker than those between atoms inside these blocks along the a-axis. This demonstrates the chemical bonding anisotropy of the studied materials.

The calculated primitive-cell volume (V) versus pressure (P) and total energy (E) versus primitive-cell volume were fitted to some different equations of states (*EOS*) to determine the bulk modulus (B) and its pressure derivative (B') for the examined systems. Figure 3 presents the fit curves of the calculated E–V and P–V data to the corresponding Birch–Murnaghan *EOS*[40] as a prototype. The obtained values of B and B' from the fitting of the calculated E–V and V–P data with the Birch–Murnaghan,[40] Murnaghan[41] and Vinet[42] *EOSs* are collected in Table II. One can appreciate the good consistency between the values of B obtained via these different versions of *EOS*. It can be observed that the value of B decreases in BaAg*Ch*F series when going in the sequence BaAgSF → BaAgSeF → BaAgTeF. This is in agreement with the known fact that the bulk modulus is inversely proportional to the primitive-cell *volume*, i.e., $B \sim V^{-1}$. The relatively small values of B of the considered materials indicate that these compounds possess a high compressibility. The computed bulk modulus values from the *EOS* fits will be employed later to examine the consistency and accuracy of the present work results by comparing them to the corresponding ones that will be

Table II. The bulk modulus (B_0, in GPa) and its pressure derivative (B', dimensionless) as extracted from Birch-Murnaghan (B.M.), Murnaghan (M.) and Vinet equation of states (*EOS*) for BaAgSF, BaAgSeF and BaAgTeF

		B.M. *EOS* fit		M. *EOS* fit		Vinet EOS fit	
Systems	**Property**	***E–V* EOS**	***P–V* EOS**	***E–V* EOS**	***P–V* EOS**	***E–V* EOS**	***P–V* EOS**
BaAgSF	B_0	60.87	61.82	60.32	62.40	61.77	61.50
	B'	4.70	4.49	4.59	4.17	4.085	4.67
BaAgSeF	B_0	55.37	56.36	54.78	56.94	55.67	56.04
	B'	4.58	4.36	4.47	4.03	4.605	4.55
BaAgTeF	B_0	46.34	45.49	45.54	46.18	46.72	45.11
	B'	4.51	4.734	4.44	4.31	4.529	4.97

Table III. Calculated single-crystal elastic constants (C_{ij}, in GPa), Bulk modulus (B, in GPa), shear modulus (G, in GPa), Young's modulus (E, in GPa), Poisson's coefficient (σ, dimensionless), Pugh's indicator (B/G), longitudinal, transversal and average sound velocities (V_l, V_t and V_m, respectively, in m/s) and Debye temperature (T_D, in K) for BaAgSF, BaAgSeF and BaAgTeF. The subscript V, R and H stand to Voigt, Reuss and Hill approximations. The compliance tensor S (S_{ij}) was calculated as the inverse of the stiffness matrix C ($S = C^{-1}$)

Property	BaAgSF	BaAgSeF	BaAgTeF
C_{11} (S_{11})	111.4 (0.0121457)	105.7 (0.0133843)	90.94 (0.0165082
C_{33} (S_{33})	77.62 (0.021210)	66.59 (0.0269921)	51.67 (0.0382949)
C_{44} (S_{44})	34.82 (0.0287206)	33.24 (0.0300857)	21.07 (0.0497541)
C_{66} (S_{66})	23.31 (0.0428973)	22.19 (0.0450560)	19.91 (0.0502173)
C_{12} (S_{12})	34.66 (−0.0008780)	33.44 (−0.0004625)	31.12 (−0.0003468)
C_{13} (S_{13})	47.18 (−0.0068492)	45.33 (−0.0087960)	39.43 (−0.0123439)
B_V	62.06	58.46	50.39
B_R	61.16	56.65	47.24
B_H	61.61	57.55	48.82
G_V	30.02	27.99	20.65
G_R	27.71	24.88	18.31
G_H	28.87	26.43	19.48
B_H/G_H	2.134	2.177	2.506
E	74.90	68.77	51.57
σ	0.2974	0.3008	0.3239
V_l	4062	3734	3329
V_t	2181	1993	1699
V_m	2435	2226	1904
T_D	266.1	238.9	196.3

derived from the single-crystal elastic parameters (C_{ij}s).

Elastic Constants and Related Properties

The calculated values of the six C_{ij} elastic constants, namely C_{11}, C_{33}, C_{44}, C_{66}, C_{12} and C_{13}, and the corresponding elastic compliances S_{ij}s for the title materials are listed in Table III. From Table III data, the following conclusions can be made:

I The computed C_{ij}s satisfy the well-known mechanical stability restrictions for tetragonal crystals.[42] Therefore, the examined compounds (including the hypothetical BaAgTeF compound) are mechanically stable.

II The difference between the values of C_{11} and C_{33} characterizes the elastic anisotropy in the stacking plane (C_{11}) and in the perpendicular [001] direction (C_{33}) in the studied systems. C_{11} is larger than C_{33}, indicating that these crystals are more resistant to compressional strains along the *a*-axis than that along the *c*-axis. This is in agreement with the fact that the bonding between the [Ag*Ch*] and [BaF] layers, stacked along the *c*-axis, is weaker than the intralayer bonding in the *ab* plane, discussed above in the "Structural properties" section. On the other hand, this result demonstrates that these materials are elastically anisotropic. One can also observe that C_{11} and C_{33} are larger than C_{44} and C_{66}, demonstrating that the resistance of the examined materials against the shear deformations is much weaker compared to that against the compressional deformations.

Table IV. Calculated acoustic wave velocities (in m/s) propagating along the [100], [110] and [001] directions in the BaAgSF, BaAgSeF and BaAgTeF systems

Direction	Polarisation	BaAgSF	BaAgSeF	BaAgTeF
[100]	[100]: v_l	4286	3984	3671
	[010]: v_{t1}	2395	2235	1767
	[001]: v_{t2}	1960	1826	1718
[001]	[001]: v_l	3577	3163	2767
	[100]: v_{t1}	1960	1826	1718
	[001]: v_{t2}	1960	1826	1718
[110]	[110]: v_l	3985	3713	3464
	[1-10]: v_{t1}	2395	2235	1767
	[001]: v_{t2}	2515	2329	2106

III Theoretically, the macroscopic mechanical properties of polycrystals, which are expressed by B and G, can be evaluated from a proper averaging of the C_{ij}s via the Voigt–Reuss–Hill approach.[34] The Voigt and Reuss averages represent the extreme limits of B and G and according to Hill,[34] the effective values of B and G can be expressed by the arithmetic mean of these two limits. The expressions of Voigt (V) and Reuss (R) approximations of B (B_R, B_V) and G (B_R, G_V) for a tetragonal structure can be found in Refs. 43 and 44. The orientation-averaged Young's modulus E and the Poisson's ratio σ can be calculated from B and G using the well-known relations.[26] The predicted values for the B, G, E and σ moduli are listed in Table IV. From Table IV data, the following conclusions can be made:

A For each considered compound, the calculated B value from the single-crystal elastic constants through the Voigt-Reuss-Hill average is in good agreement with the corresponding one derived from the *EOS* fit. Therefore, this good agreement between the B values obtained via two different computational methods constitutes another proof of the reliability and accuracy of the computed elastic moduli.

B The considered compounds have a relatively small Young's modulus (E) value. This confirms the rather low stiffness of the considered compounds. As E characterizes the resistance of a solid against uniaxial deformation, so it is related to C_{11} and C_{33} elastic constants, which explains the decrease of E when going from BaAgSF to BaAgSeF to BaAgTeF in the same sequence as C_{11} and C_{33}. The shear modulus G decreases also when going from BaAgSF to BaAgSeF to BaAgTeF in accordance with the decrease of the C_{44}.

C According to an empirical criterion by Pugh,[45] a solid is brittle (ductile) if the B/G ratio is smaller (greater) than 1.75. The B/G ratios of all herein studied compounds are greater than 1.75, suggesting their ductile behaviour. A ductile material is resistant to thermal shocks. The bulk modulus B is two times the shear modulus G, indicating that the shear deformation is easier to occur in the considered compounds.

IV It is established that the anisotropy of the coefficient of thermal expansion and elastic anisotropy can cause microcracks in materials.[46] It is also accepted that the elastic anisotropy can significantly influence the nanoscale precursor textures in alloys.[47] Therefore, it becomes necessary and important to estimate the elastic anisotropy extent in solids. Some different indices have been established to estimate the elastic anisotropy degree in crystals. To evaluate the elastic anisotropy degree in the considered BaAg*Ch*F compounds, two different approaches were employed.

1. Ranganathan and Ostoja-Starzewski[48] proposed a universal index A^U, defined as follows $A^U = 5G_V/G_R + B_V/B_R - 6$, to quantify the elastic anisotropy extent in a crystal. An isotropic crystal is characterized by $A^U = 0$. Any deviation of A^U from zero indicates the presence of an elastic anisotropy and the degree of this deviation gives the extent of this elastic anisotropy. The computed values of the A^U ($A^U = 0.43$ for BaAgSF, $A^U = 0.66$ for BaAgSeF and $A^U = 0.71$ for BaAgTeF) demonstrate that the considered compounds exhibit a noticeable elastic anisotropy and its degree increases when going from BaAgSF to BaAgSeF to BaAgTeF.
2. A more used tool to visualize the elastic anisotropy extent of crystals is by plotting three-dimensional (3-D) representations of the directional dependence of their elastic moduli. 3-D representations of the directional dependence of the Young's modulus E and compressibility β ($\beta = 1/B$) were used in the present work. For a tetragonal

crystal, the crystallographic direction dependence of the Young's modulus E and compressibility β are expressed by the following relations[49]:

$$\frac{1}{E} = (l_1^4 + l_2^4)s_{11} + l_3^4 s_{33} + l_1^2 l_2^2(2s_{12} + s_{66}) + l_3^2(1 - l_3^2)(2s_{13} + s_{44}) \tag{1}$$

$$\beta = (s_{11} + s_{12} + s_{13}) + l_3^2(s_{11} + s_{12} - s_{13} - s_{33}). \tag{2}$$

In Eqs. 1 and 2, S_{ij}s are the elastic compliance constants and l_1, l_2 and l_3 are the directional cosines with respect to the x-, y- and z- axes, respectively. In a closed 3D-representation, the distance from the origin of the coordination system to the surface gives the value of the represented modulus in a given direction. Thus, for an isotropic material, the representative closed surface should exhibit a spherical shape. Any deviation of the representative closed surface from the spherical shape announces the presence of an elastic anisotropy.[50] From Figs. 3 and 4, one can appreciate that the shape of the 3D-closed surfaces for E and β are considerably different from the spherical shape, suggesting a strong elastic anisotropy of the examined materials. The cross-sections of the 3D-closed surface of the E modulus in the xy and xz planes are also represented in Fig. 3 in order to more visualize the elastic anisotropy. These 2D-representations clearly show the pronounced elastic anisotropy of the considered systems. The highest value of the Young's modulus ($E_{\max}$) is realized for applied external stress along the [100] and [010] crystallographic directions, and the lowest value of the Young's modulus $E_{\min}$ is along the [001] direction, which is consistent with the fact that the a-axis is more resistant against compression than the c-axis. The $E_{\min}$ is approximately 57% $E_{\max}$ in BaAgSF, 49% $E_{\max}$ in BaAgSeF and 43% $E_{\max}$ in BaAgTeF, which indicates that the elastic anisotropy degree increases when going from BaAgSF to BaAgSeF to BaAgTeF.

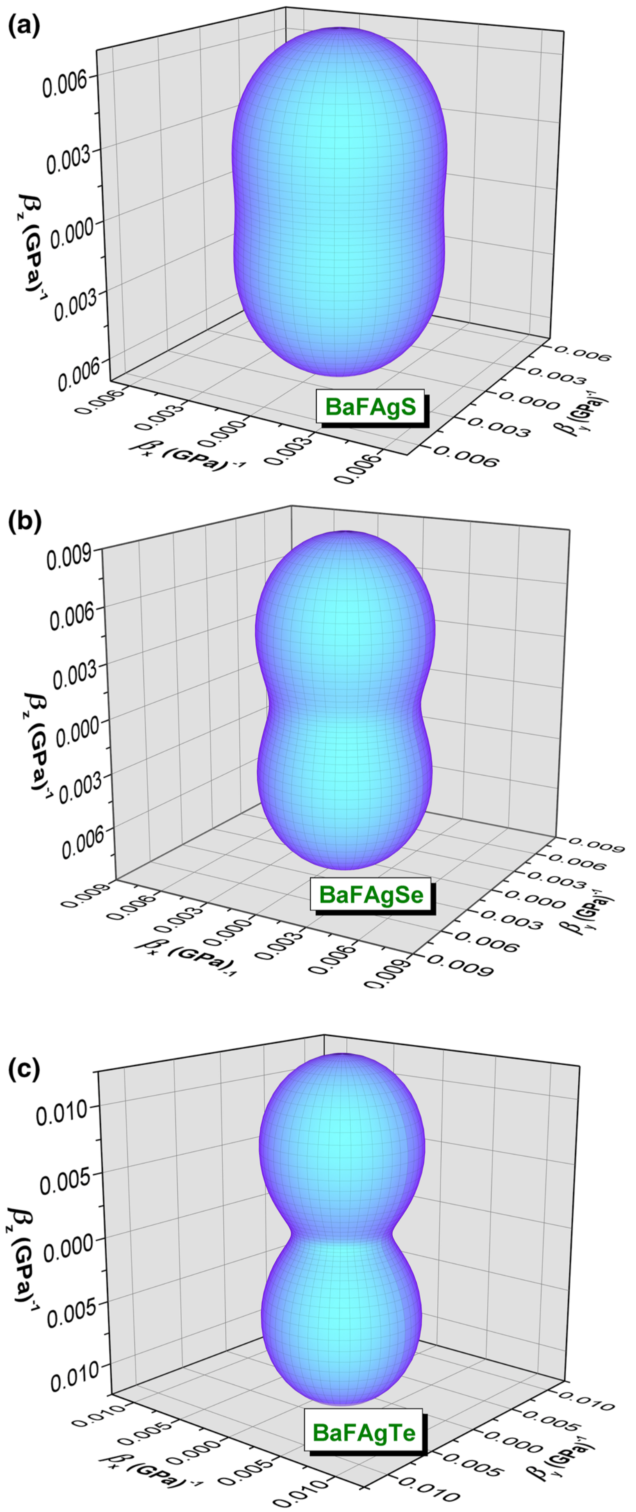

Fig. 4. The compressibility (β) 3D-representation for BaAgSF (a), BaAgSeF (b) and BaFAgTe (c).

V One can calculate the Debye temperature (T_{D}), which is correlated with many important fundamental physical properties of solids, from the computed B and G moduli as follows[51]:

$$T_{\mathrm{D}} = \frac{h}{k_{\mathrm{B}}}\left[\frac{3n}{4\pi V_{\mathrm{a}}}\right]^{1/3} V_{\mathrm{m}}. \tag{3}$$

Here, h is Plank's constant, k_{B} is Boltzmann's constant, n is the number of atoms in the molecule, and V_{a} is the atomic volume. The average sound wave velocity V_{m} in a polycrystalline material is given by[52]:

$$V_m = \left[\frac{1}{3}\left(2V_t^{-3} + V_l^{-3}\right)\right]^{-1/3}. \quad (4)$$

In Eq. 4, V_l and V_t are the transverse and longitudinal elastic waves in the polycrystalline phase of material, respectively, which are given by the Navier's equations:

$$V_l = \left(\frac{3B + 4G}{3\rho}\right)^{1/2}, \quad V_t = \left(\frac{G}{\rho}\right)^{1/2}. \quad (5)$$

Here, ρ is the mass density. Calculated T_D and average sound wave velocities (V_l, V_t and V_m) values are listed in Table III. The T_D value decreases when going from BaAgSF to BaAgSeF to BaAgTeF, which is an accordance with the decreases of the stiffness in the same sequence. This might indicate a decrease of the thermal conductivity when going from BaAgSF to BaAgSeF to BaAgTeF.

VI The sound wave velocities are related to some physical properties of crystals such as the thermal conductivity. In a tetragonal crystal, the elastic wave velocities propagating along the [100], [001] and [110] crystallographic directions can be calculated using the known relationships given in Ref. 53. The obtained elastic wave velocities are gathered in Table IV. The longitudinal wave velocities are larger than the transverse ones and both the longitudinal and transverse waves decrease when going from BaAgSF to BaAgSeF to BaAgTeF. This can be explained by the decease of the single-crystal elastic constants in the same sequence; the elastic wave velocities are proportional to the square root of the corresponding elastic constants.

Electronic Band Dispersion and Density of States

Figure 5 shows the calculated GGA08 and TB-mBJ energy band dispersions along some high symmetry lines of the BZ for the BaAgSF, BaAgSeF and BaAgTeF systems at the equilibrium lattice parameters obtained using the FP-LAPW method with the GGA08 (see Table I). Both the upper valence band maximum (UVBMa) and lower conduction band minimum (LCBMi) occur at the center of the BZ, demonstrating that these compounds are direct energy band gap (Γ–Γ) semiconductors. For all investigated compounds, the overall profile of the GGA08 band structure is almost similar to that of the TB-mBJ one. There is an important quantitative difference between the TB-mBJ band gap and the GGA08 one; the obtained TB-mBJ (GGA08) fundamental band gap is 2.89 eV (1.47 eV) for BaAgSF, 2.66 eV (1.22 eV) for BaAgSeF and 2.56 eV (1.56 eV) for BaAgTeF. The TB-mBJ displaces the conduction bands toward higher energies with respect to the top of the valence band, so, the TB-mBJ band gap is larger than the GGA08 one. No experimental data concerning the band gaps of the title materials are available in the literature to be compared with our results. Our calculated GGA08 band gaps for BaAgSF and BaAgSeF are in acceptable agreement with the available theoretical results,[12] which were performed using the FP-LAPW method within the GGA96. If we bear in mind that the GGA DFT band gap is approximately 30–50% smaller than the corresponding experimental one,[23–25] we can expect that the real band gaps of the considered materials will be larger than those obtained using the GGA08. From Table V, one can appreciate that the TB-mBJ approach improves the band gap values of BaAgSF, BaAgSeF and BaAgTeF by approximately 49%, 54%, and 40%, respectively, compared to the corresponding GGA08 ones. Therefore, the calculated TB-mBJ band gaps might be expected to be in reasonable agreement with the real values. The TB-mBJ band gaps for the BaAg*Ch*F series, expanding in the energy interval from 2.6 eV to 2.9 eV, are comparable with the measured gaps for the isostructural SrCuSF (3.0 eV) and SrCuSeF (2.7 eV).[54] Owing to the advantages of the TB-mBJ, we report and discuss only the results obtained within the TB-mBJ potential in the rest of the manuscript. One can note that the overall profile of the band structure dispersions of the BaAgSF and BaAgSeF compounds are practically identical, whereas that of BaAgTeF is somewhat different; for example, the lower valence band group in BaAgSF and BaAgSeF (Fig. 5) splits into two distinct narrow band groups in BaAgTeF. The width of the near-Fermi level valence band group increases slightly when the *Ch* chalcogen atom in the BaAg*Ch*F series is replaced in the following sequence: S → Se → Te, indicating a slight increase of the ionic character. One can observe narrow quasi-flat valence bands along the Γ–Z, A–M and R–X lines of the BZ, which correspond to the crystallographic *c*-axis, and relatively broad large dispersive valence bands along the Z–A, Γ–M, Z–R and Γ–X directions of the BZ, which are in the *ab* plane of the crystal. These behaviours demonstrate the high anisotropy of the chemical bonding in the layered BaAg*Ch*F systems; the chemical bonding inside the blocks [BaF] and [Ag*Ch*] differs considerably from the inter-adjacent-blocks bonding. Similar behaviours of the high-energy valence bands, i.e., the coexistence of quasi-flat and relatively high dispersive valence bands, were reported for other 1111-like oxychalcogenides and fluorochalcogenides.[5,6,12,21,54] These features are considered as favourable indicators of high *p*-type conductivity, promoting a relatively high hole mobility and a high hole concentration.[12,54]

The total (TDOS) and atomic-resolved *l*-projected (PDOS) densities of electronic states diagrams help to assign the electronic states of the electronic energy bands. The calculated TDOS and PDOS diagrams for the BaAgSF, BaAgSeF and BaAgTeF

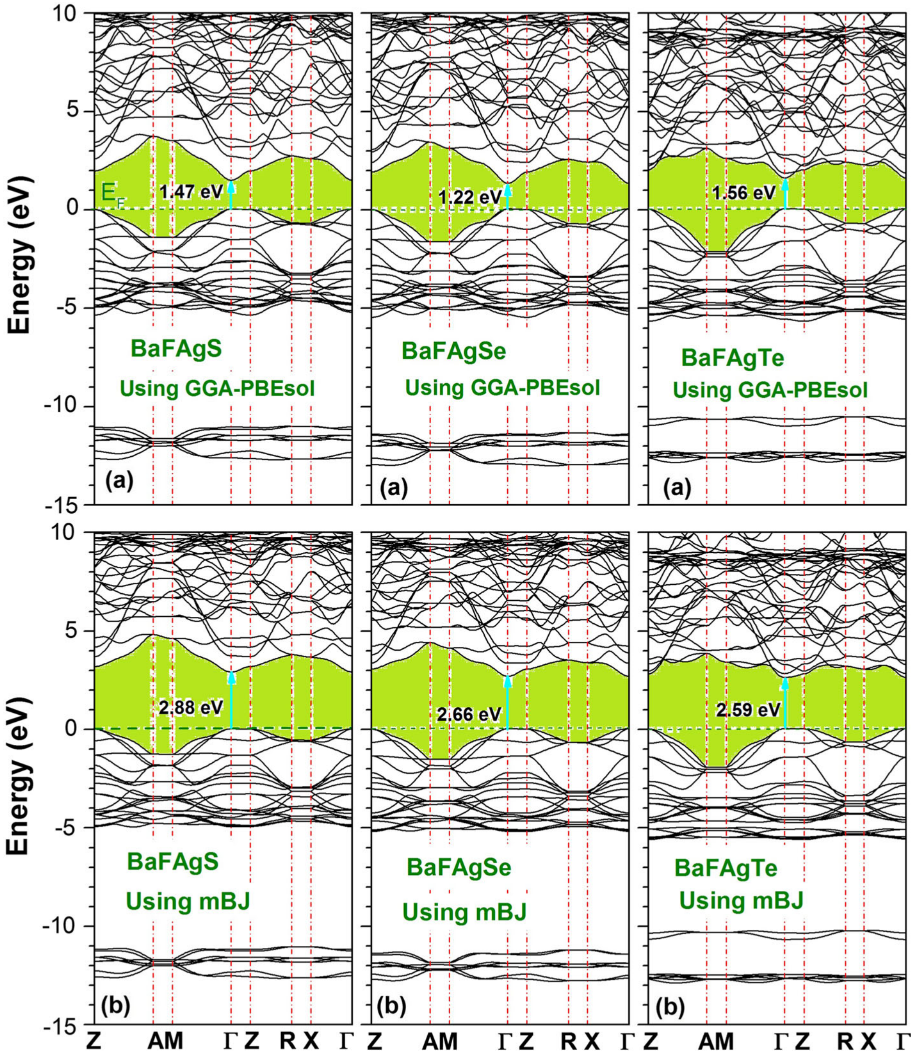

Fig. 5. GGA-PBEsol (a) and TB-mBJ (b) band structures of the BaAgSF, BaAgSeF and BaAgTeF systems along some high-symmetry lines in the Brillouin zone. The energy zero level corresponds to the Fermi level.

Table V. Calculated energy band gaps (E_g, in eV) within the GGA-PBEsol (GGA08) and TB-mBJ approximations compared to the available theoretical results

System	E_g (Γ–Z)	E_g (Γ–A)	E_g (Γ–M)	E_g (Γ–Γ)	E_g (Γ–R)	E_g (Γ–X)
BaFAgS						
GGA08[a]	2.002	3.674	3.427	1.516	2.742	2.605
GGA08[b]	1.939	3.700	3.477	1.468	2.800	2.571
TB-mBJ[b]	3.170	4.791	4.591	2.886	3.774	3.651
Other[12]				1.387		
BaFAgSe						
GGA08[a]	1.912	3.390	3.053	1.323	2.554	2.414
GGA08[b]	1.875	3.397	3.082	1.218	2.379	2.515
TB-mBJ[b]	3.025	4.364	4.099	2.663	3.486	3.351
Other[12]				1.278		
BaFAgTe						
GGA08[a]	1.999	2.989	2.438	1.534	2.346	2.202
GGA08[b]	1.974	3.070	2.551	1.557	2.364	2.227
TB-mBJ[b]	2.774	3.818	3.378	2.595	3.170	3.021

[a] Present, using CASTEP code. [b] Present, using WIEN2K code.

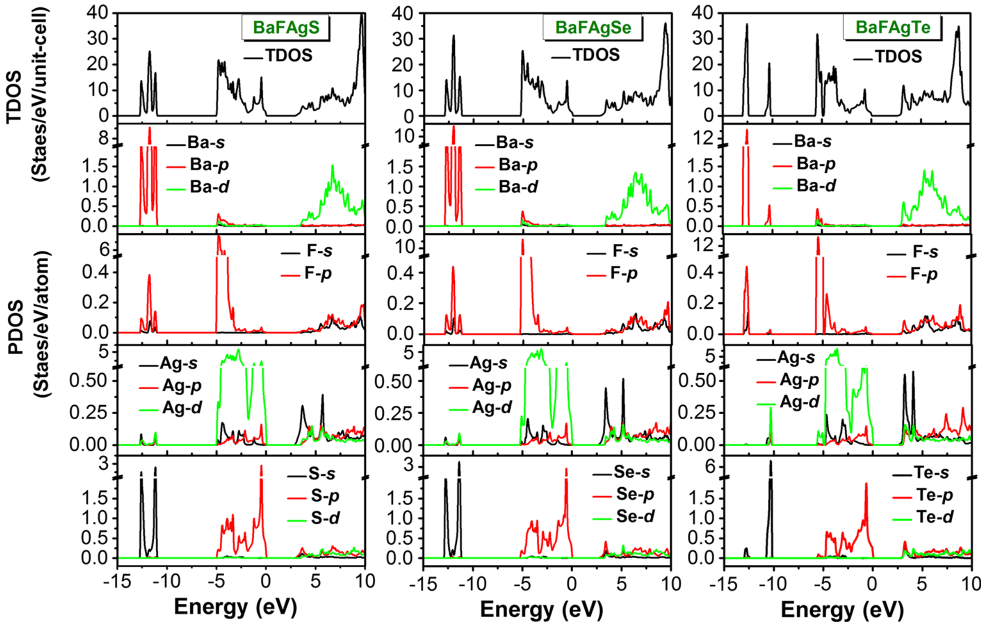

Fig. 6. The total and atomic-resolved *l*-decomposed densities of states (TDOS and PDOS, respectively) for the BaAgSF, BaAgSeF and BaAgTeF systems. The energy zero level corresponds to the Fermi level.

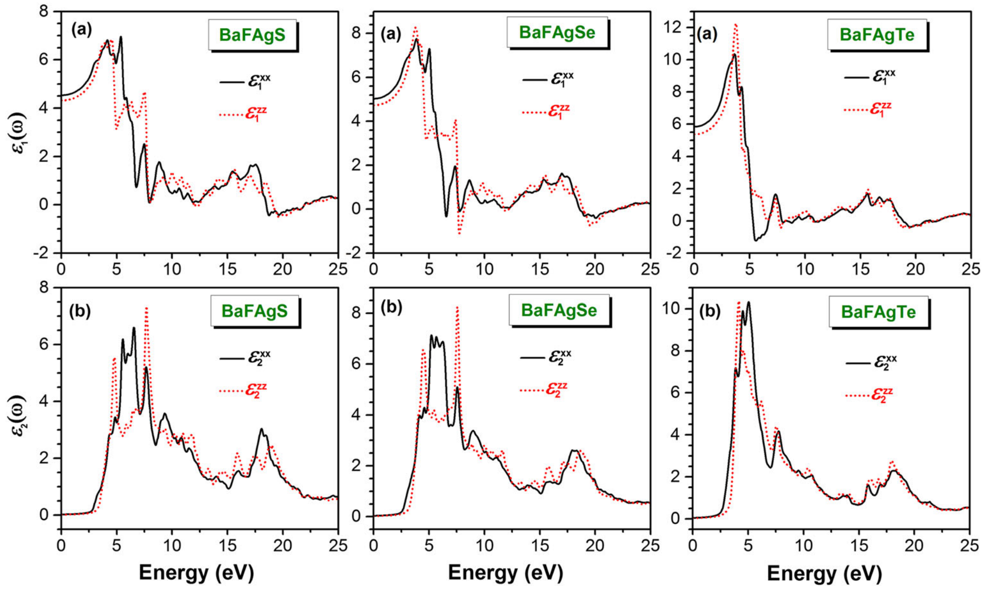

Fig. 7. The frequency-dependent imaginary ($\varepsilon_2(\omega)$ (b)) and real ($\varepsilon_1(\omega)$ (a)) parts of the dielectric function tensor components for the BaAgSF, BaAgSeF and BaAgTeF systems.

compounds are depicted in Fig. 6. Three narrow band valence groups centred at about ∼−54, ∼−26 and ∼−24 eV, which are not shown in Fig. 6 for clarity of the diagrams, are mainly formed from the 4*p*-Ag, 5*s*-Ba and 2*s*-F states, respectively. The lower valence band group (Fig. 6) in the BaAgSF and BaAgSeF DOS spectra exhibits three well-distinguished peaks that are made predominantly of the 5*p*-Ba and n*s*-chalcogen states ($n = 3$ for S, $n = 4$ for Se and $n = 5$ for Te) with a small contribution from the 2*p*-F states. In the BaAgTeF DOS diagram, this valence band group splits into two groups clearly separated by an energy gap because the 5*s*-Te states are located somewhat higher in energy than the 5*p*-Ba ones. The upper valence band group (UVB), which is extended from approximately −5.5 eV to Fermi level E_F, is formed of two main structures. The lower structure of the UVB, ranging from approximately −5.5 eV to −2.0 eV, is formed from the 4*d*-Ag, 2*p*-F and n*p*-

Ch states and the higher one, which is extended approximately from -2.0 eV to E_F, is attributed to the 4*d*-Ag states well mixed with n*p*-*Ch* states ($n = 3$ for S, $n = 4$ for Se and $n = 5$ for Te). The hybridization of the n*p*-*Ch* and 4*d*-Ag states suggests that the *Ch*-Ag bonds inside the blocks [Ag*Ch*] are mainly covalent. On the other hand, from the PDOS diagrams, one can easily observe the weak contribution of the Ba states in the UVB group, whereas a consistent contribution of the fluorine states is localised in the bottom of this valence band group. Consequently, the overlapping of Ba and F states is quite weak, indicating that the Ba-F chemical bonding inside the [BaF] blocks is mainly of ionic character. The bottom of the conduction band is attributed to an admixture of the n*s*-*Ch*, 4*sp*-Ag and 5*sd*-Ba states.

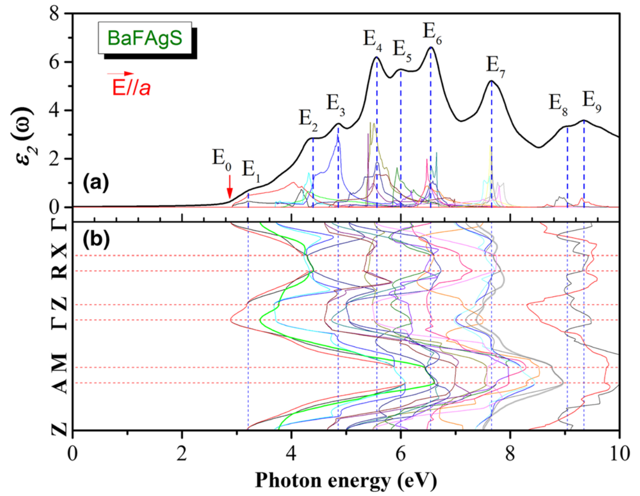

Fig. 8. Decomposition of the imaginary part of the dielectric function $\varepsilon_2^{xx}(\omega)$ into band-to-band contribution (upper panel a) and the transition energy band structure (lower panel b) for BaAgSF. The counting of the bands is down (up) from the top (bottom) of the valence (conduction) band.

Optical Properties

The calculated frequency-dependent dispersive ($\varepsilon_1(\omega)$) and absorptive ($\varepsilon_2(\omega)$) parts of the dielectric function ($\varepsilon(\omega)$) for the BaAgSF, BaAgSeF and BaAgTeF systems are depicted in Fig. 7. Due to the tetragonal symmetry of the title materials, only the diagonal dielectric tensor components, namely $\varepsilon^{xx} = \varepsilon^{yy}$ and ε^{zz}, are non-zero. The dielectric tensor component $\varepsilon^{xx}(\varepsilon^{yy})$ corresponds to the electric fields $\vec{E}$ of the incident radiation parallel to the *x*-axis (*y*-axis) (i.e., $\vec{E}//\vec{a}$ ($\vec{E}//\vec{b}$)) and to the *z*-axis (i.e., $\vec{E}//\vec{c}$). In view of Fig. 7, one can observe the following features: First, there are noticeable differences between the magnitudes, shapes and locations of the main peaks in the $\varepsilon_2^{xx}(\omega)(\vec{E}//\vec{a})$ and $\varepsilon_2^{zz}(\omega)$ $(\vec{E}//\vec{c})$, revealing a strong anisotropy of the dielectric response of the examined systems to the incident radiation. Second, the overall shape of the dielectric

Table VI. Peak positions of the $\varepsilon_2^{xx}(\omega)$ spectrum together with the dominant interband transition contributions to every peak and their location in the Brillouin zone for the BaFAgS compound

Optical structures		Dominant interband transition contributions		
Structure	**Peak position**	**Transition**	**Region**	**Energy (eV)**
E_1	3.21	V2–C1	Z, M–Γ, Z–R, X–Γ	3.21
E_2	4.39	V1–C1	Z, M–Γ, Z–R, X–Γ	3.19
		V1–C2	Z–A, M–Γ	4.30
		V1–C2	Z–A, M–Γ	4.29
E_3	4.86	V2–C2	Z–A, M–Γ	4.85
E_4	5.56	V4–C3	Z–A, M–Γ, X–Γ	5.51
		V4–C2	Z–A, M–Γ	5.57
		V2–C4	Z–A, M–Γ, Z–R	5.51
		V1–C4	Z–A, M–Γ, Z–R	5.53
E_5	6.00	V2–C5	Z–A, M–Γ, Γ–Z, Z–R, X–Γ	5.94
E_6	6.54	V6–C1	Z–A, A–M, M–Γ, Z–R, X–Γ	6.64
		V5–C2	Z–A, A–M, M–Γ, Z–R, X–Γ	6.60
		V4–C5	Z–R, R–X, X–Γ	6.49
		V1–C6	Z–A, M–Γ, Z–R, R–X, X–Γ	6.56
		V1–C8	Z–A, M–Γ, Γ–Z, Z–R, X–Γ	6.47
E_7	7.66	V16–C1	Z–A, M–Γ, Z–R, X–Γ	7.78
		V15–C1	Z–A, M–Γ, Z–R, X–Γ	7.68
		V14–C1	Z–A, M–Γ, Z–R, R–X, X–Γ	7.63
		V13–C1	Z–A, M–Γ, Z–R, R–X	7.62
		V5–C3	Z–A, M–Γ, Z–R, X–Γ	7.79
E_8	9.05	V10–C5	Z–A, M–Γ, Z–R, X–Γ	8.88
E_9	9.35	V1–C16	Z–A, M–Γ, Z–R, X–Γ	9.31

Table VII. Peak positions of the $\varepsilon_2^{zz}(\omega)$ spectrum together with the dominant interband transition contributions to every peak and their location in the Brillouin zone for the BaFAgS compound

Optical structures		Dominant interband transition contributions		
Structure	**Peak position**	**Transition**	**Region**	**Energy (eV)**
E_1	7.69	V2–C1	Z–A, M–Γ, Z–R, X–Γ	4.17
		V3–C2	Z–A, M–Γ, Z–R, X–Γ	4.04
E_2	4.78	V1–C2	Z–A, M–Γ, Z–R, X–Γ	4.90
		V1–C3	Z–A, M–Γ	4.70
		V4–C4	Z–A, M–Γ, Z–R, X–Γ	4.78
E_3	5.86	V1–C5	Z–A, M–Γ	5.94
		V1–C6	Z–A, M–Γ, Γ–Z, Z–R, X–Γ	5.79
		V2–C5	Z–R, X–Γ	5.86
		V4–C5	Z–A, M–Γ, Γ–Z, Z–R, X–Γ	5.90
E_4	6.46	V2–C7	M–Γ, Z–R, X– Γ	6.47
		V3–C6	Z–A, M–Γ, Γ–Z, Z–R, X–Γ	6.43
		V3–C5	Z–A, M–Γ, Z–R, X– Γ	6.42
		V3–C7	Z–A, M–Γ, Γ–Z, Z–R, X–Γ	6.41
		V7–C4	Z–A, Z–R	6.45
E_5	6.87	V6–C2	Z–A, M–Γ	6.87
		V2–C8	Z–A, M–Γ	6.79
		V3–C8	Z–A, M–Γ, Z–R, X–Γ	7.12
		V1–C9	Z–A, M–Γ, Z–R, X–Γ	6.74
		V15–C1	Z–A, M–Γ, Z, Z–R	6.87
E_6	7.69	V14–C1	Z–A, M–Γ, Z–R, X	7.64
		V13–C1	Z–A, M–Γ, Z–R, R–X	7.63
		V5–C4	Z–A, M–Γ, Z–R, R–X	7.73
		V5–C6	Z–A, M–Γ, Z–R, X–Γ	7.82
E_7	8.64	V12–C3	Z–A, M–Γ, Z–R, X–Γ	8.65
E_8	9.35		Z–A	9.29

Table VIII. Peak positions of the $\varepsilon_2^{xx}(\omega)$ spectrum together with the dominant interband transition contributions to every peak and their location in the Brillouin zone for the BaFAgSe

Optical structures		Dominant interband transition contributions		
Structure	**Peak position**	**Transition**	**Region**	**Energy (eV)**
E_1	4.15	V3–C1	Z–A, M–Γ, Z–R, R–X, X–Γ	4.19
		V2–C2	Z–A, M–Γ, Z–R, R–X, X–Γ	4.11
		V1–C1	Z–A, M–Γ, Z, R–X	4.13
E_2	4.59	V3–C2	Z–A, M–Γ, Z–R, X–Γ	4.65
		V2–C2	Z–A, M–Γ, Z–R	4.57
E_3	5.21	V4–C2	Z–A, M–Γ, Z–R	5.20
		V4–C3	Z–A, Γ–Z, Z–R, X–Γ	5.16
		V2–C3	Z–A, M–Γ	5.19
		V1–C4	Z–A, M–Γ, Z–R, X–Γ	5.18
E_4	5.65	V4–C4	Z–A, M–Γ, Z–R, X–Γ	5.60
		V3–C5	Z–A, Z–R, X–Γ	5.71
		V2–C5	Z–A, M–Γ, Γ–Z, Z–R, X–Γ	5.62
		V1–C3	Z–A, M–Γ	5.64
E_5	6.25	V5–C2	Z–A, M–Γ, Z–R, X–Γ	6.31
		V4–C5	Z–R, R–X, X	6.27
		V1–C6	Z–A, M– Γ, Z–R, R–X, X–Γ	6.24
E_6	6.98	V5–C5	Z–A, M–Γ, Γ–Z, Z–R, X–Γ	6.95
		V3–C3	Z–A, M–Γ	6.98
E_7	7.55	V15–C2	R–X, X–Γ	7.59
		V14–C1	Z–A, M–Γ, Z–R, R–X, X–Γ	7.60
		V13–C1	Z–A, M–Γ, Z–R, R–X	7.49
E_8	8.99	V13–C3	Z–A, A–M, M–Γ	9.00
		V1–C15	Z–A, M–Γ, Z–R, X–Γ	9.01

Table IX. Peak positions of the $\varepsilon_2^{zz}(\omega)$ spectrum together with the dominant interband transition contributions to every peak and their location in the Brillouin zone for the BaFAgSe compound

Optical structures		Dominant interband transition contributions		
Structure	**Peak position**	**Transition**	**Region**	**Energy (eV)**
E_1	3.99	V1–C2	Z–A, M–Γ, Z–R, X–Γ	4.00
		V2–C1	Z–A, M–Γ, Z–R, X–Γ	4.03
E_2	4.03	V3–C2	Z–A, M–Γ, Z–R, X–Γ	4.62
		V1–C2	Z–A, M–Γ	4.42
		V2–C3	Z–A, M–Γ, Z–R, X–Γ	4.44
E_3	5.43	V2–C4	Z–A, M–Γ, Z–R	5.41
		V2–C5	Z–A	5.54
		V1–C5	Z–A, Z–R, X–Γ	5.40
		V1–C6	Z–R, X–Γ	5.45
E_4	6.19	V3–C4	Z–A, M–Γ	6.22
		V3–C5	Z–A, M–Γ, Z–R, R, X–Γ	6.22
		V3–C6	Z–A, M–Γ, Z–R, R, X–Γ	6.21
		V3–C7	M–Γ, Z–R	6.19
E_5	6.49	V6–C2	Z–A, M–Γ	6.76
		V3–C8	Z–A, M–Γ, Z–R, X–Γ	6.44
		V2–C8	Z–A, M–Γ, Z–R, X–Γ	6.48
		V1–C9	Z–A, M–Γ, Z–R, X–Γ	6.48
E_6	6.82	V7–C4	Z–A, M–Γ, Z–R, X–Γ	6.78
		V2–C9	Z–A, M– Γ, Z–R, X– Γ	6.76
		V1–C10	Z–A, M–Γ, Z–R, X–Γ	6.84
E_7	7.55	V15–C1	Z–A, M–Γ, Z–R, R–X, X–Γ	7.60
		V14–C1	Z–A, M–Γ, Z–R, R–X, X–Γ	7.58
		V13–C1	Z–A, M–Γ, Z–R, R–X	7.54
		V5–C4	Z–A, Z–R, R–X, X–Γ	7.49
E_8	8.37	V4–C12	Z–A, Z–R, X–Γ	8.39
E_9	8.88	V12–C3	Z–A, M–Γ, Z–R	8.95
		V11–C3	Z–A, M–Γ	8.87
		V11–C5	Z–A, M–Γ, Z–R, R–X, X–Γ	8.95
		V3–C16	Z–A, M–Γ, Z–R, X–Γ	8.89
E_{10}	9.21	V5–C11	Z–A, M–Γ, Z–R, X–Γ	9.23

Table X. Peak positions of the $\varepsilon_2^{xx}(\omega)$ spectrum together with the dominant interband transition contributions to every peak and their location in the Brillouin zone for the BaFAgTe compound

Optical structures		Dominant interband transition contributions		
Structure	**Peak position**	**Transition**	**Region**	**Energy (eV)**
E_1	3.88	V2–C1	Z–A, M–Γ, Z–R, X–Γ	3.81
		V2–C2	Z–A, M–Γ, Z–R, X–Γ	3.89
		V1–C2	Z–A, M–Γ	3.86
		V1–C1	Z–A, M–Γ	3.86
E_2	4.50	V4–C3	Z–R, X–Γ	4.45
		V4–C2	Z–A, M–Γ, Z–R, X–Γ	4.51
		V3–C3	Γ–Z	4.44
		V2–C3	Z–A, M–Γ	4.50
		V1–C4	Z–A, M–Γ, Z–R, X–Γ	4.55
E_3	5.05	V3–C4	Z–A, M–Γ, Z–R, X–Γ	4.99
		V3–C3	Z–A, M–Γ	5.04
		V2–C3	Z–A, M–Γ	5.04
		V2–C5	Z–A, M–Γ, Z–R, X–Γ	5.13
		V1–C7	M–Γ, Z–R, X–Γ	5.13
E_4	7.74	V16–C1	Z–A, M–Γ, Z–R, X–Γ	7.83
		V16–C2	Z–A, M–Γ, Γ–Z, Z–R, X–Γ	7.78
		V15–C1	Z–A, M–Γ, Z–R, X–Γ	7.78
		V15–C2	Z–A, M–Γ, Z–R, X–Γ	7.72

Table XI. Peak positions of the $\varepsilon_2^{zz}(\omega)$ spectrum together with the dominant interband transition contributions to every peak and their location in the Brillouin zone for the BaFAgTe compound

Optical structures		**Dominant interband transition contributions**		
Structure	**Peak position**	**Transition**	**Region**	**Energy (eV)**
E_1	4.15	V4–C1	M–Γ, Γ–Z, Z–R, X–Γ	4.07
		V2–C2	Z–A, M–Γ	4.13
		V2–C1	Z–A, M–Γ	4.15
		V2–C3	Z–A, M–Γ, Z–R, X–Γ	4.18
		V1–C2	Z–A, M–Γ	4.14
E_2	4.59	V4–C3	Γ–Z, Z–R, X–Γ	4.55
		V3–C3	Z–A, M–Γ	4.60
		V1–C5	Z–R, X–Γ	4.53
		V1–C4	Z–A, M–Γ, Z–R	4.60
		V1–C2	Z–A, M–Γ	4.56
E_3	5.05	V2–C6	Z–A, M–Γ, Γ–Z, Z–R, X–Γ	5.06
		V2–C1	Z–A, M–Γ	5.08
		V1–C5	Z–A, M–Γ, Z–R, X–Γ	5.06
E_4	5.51	V3–C6	Z–A, M– Γ, Γ –Z, Z–R, R–X, X– Γ	5.47
		V3–C3	Z–A, M–Γ	5.50
		V3–C7	Z–A, M–Γ, Z–R, X–Γ	5.49
		V2–C7	Z–A, M–Γ, Z–R, X–Γ	5.51
		V2–C8	Z–A, M–Γ, Γ–Z, Z–R, X–Γ	5.57
E_5	6.16	V3–C3	Z–A, M–Γ	6.19
		V3–C4	Z–A, M–Γ	6.19
		V2–C9	Z–A, M–Γ, Z–R, R–X, X–Γ	6.15
E_6	7.52	V15–C1	Z–A, M–Γ, Z–R, R, X–Γ	7.48
		V14–C2	A–M, M–Γ, Γ–Z, Z–R, X–Γ	7.63
		V14–C1	Z–A, A–M, M–Γ, Z–R, X–Γ	7.47
		V13–C1	Z–A, A–M, M–Γ, Z–R, X–Γ	7.56
		V13–C2	A–M, M–Γ, Γ–Z, Z–R, X–Γ	7.47

Table XII. Calculated static dielectric constant $\varepsilon_1(0)$ and, static refractive index and static optical reflectivity for BaFAgS, BaFAgSe and BaFAgTe as calculated using the TB-mBJ for two different polarizations of the incident radiations, compared with the available data in the scientific literature

System	$\varepsilon_1^{xx}(\mathbf{0})$	$\varepsilon_1^{zz}(\mathbf{0})$	$\boldsymbol{n}^{xx}(\mathbf{0})$	$\boldsymbol{n}^{zz}(\mathbf{0})$	$\boldsymbol{R}^{xx}(\mathbf{0})$	$\boldsymbol{R}^{zz}(\mathbf{0})$
BaFAgS	4.53 5.22[12]	4.33 4.89[12]	2.13	2.08	13.0	12.0
BaFAgSe	5.03	4.74	2.24	2.17	14.6	13.6
BaFAgTe	5.85	5.37	2.42	2.32	17.2	15.8

function spectra of BaAgSF and BaAgSeF are almost similar, whereas that of BaAgTeF is somewhat different from them. This difference can be attributed to the fact that the energy band dispersion of BaAgTeF is somewhat different from those of BaAgSF and BaAgSeF. Third, the intensity of the peaks increases when we move in the following sequence: BaAgSF → BaAgSeF → BaAgTeF. The $\varepsilon_2^{xx}(\omega)$ and $\varepsilon_2^{zz}(\omega)$ spectra start at the same energy (E_0), indicating an isotropic energy gap. However, $\varepsilon_2^{xx}(\omega)$ and $\varepsilon_2^{zz}(\omega)$ grow with different rates. To access the electronic transitions that are responsible for the peaks observed in the $\varepsilon_2(\omega)$ spectra, the $\varepsilon_2(\omega)$ spectrum is decomposed to the individual contribution from each electronic transition from the occupied valence band V_i to the unoccupied conduction band C_j, i.e., determination of the contribution of each allowed electronic transition ($V_\mathrm{i} \rightarrow C_\mathrm{j}$) to the $\varepsilon_2(\omega)$ spectrum. To determine which electronic states of the bands V_i and C_j are involved in the $V_\mathrm{i} \rightarrow C_\mathrm{j}$ transition, the electronic transition energies $E_\mathrm{ij}(k)$ $(E_\mathrm{ij}(k) = E_{\mathrm{C_j}}(k) - E_{\mathrm{V_i}}(k))$ are plotted along the high-symmetry directions of the BZ. For sake of brevity, only decomposition of the $\varepsilon_2^{xx}(\omega)$ spectrum of BaAgSF to individual contributions of the electronic transitions ($V_\mathrm{i} \rightarrow C_\mathrm{j}$) and the corresponding transition energy $E_\mathrm{ij}(k)$ dispersion are shown in Fig. 8, as representative for the other studied systems. The first threshold energy E_0 of $\varepsilon_2(\omega)$, termed also the fundamental absorption edge,

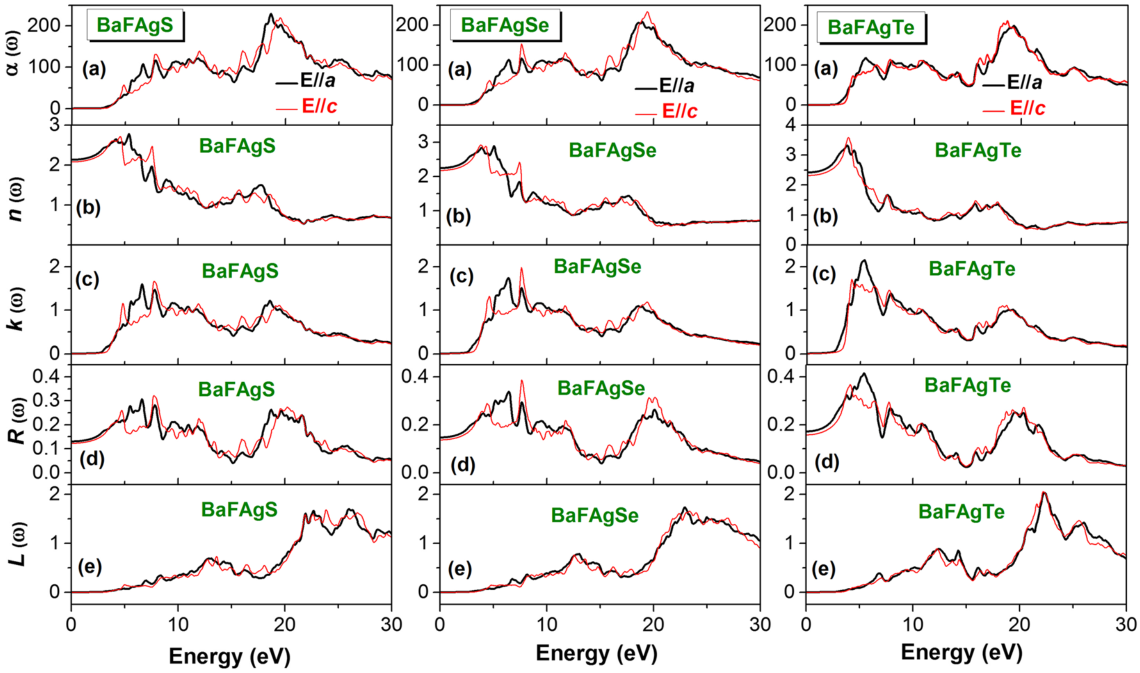

Fig. 9. Frequency-dependent absorption coefficient ($\alpha(\omega)$ (a)), refractive index ($n(\omega)$(b)), extinction coefficient ($k(\omega)$ (c)), optical reflectivity ($R(\omega)$(d)) and energy-loss function ($L(\omega)$(e)) spectra for BaAgSF, BaAgSeF and BaAgTeF systems for two different light polarizations as calculated using the TB-mBJ potential.

is originated from the direct electronic transition between the topmost valence band V_1 and the bottommost conduction band C_1 ($V_1 \rightarrow C_1$). It is to be noted that the bands counting is up (down) from the bottommost (topmost) of the conduction (valence) band. The locations of the major peaks E_i (i = 1, 2…etc.) and the origin of the dominant optical transitions in an energy range up to 10 eV are listed in Tables VI, VII, VIII, IX, X, and XI. The obtained electronic static dielectric constant $\varepsilon^e(0) = \varepsilon_1$ $(\omega \rightarrow 0)$, which is a parameter of fundamental importance in many aspects of material properties, is given in Table XII. Our results are in agreement with the available theoretical results for BaAgSF.[12] The $\varepsilon_1(0)$ increases in the following sequence: BaAgSF $\rightarrow$ BaAgSeF $\rightarrow$ BaAgTeF and the ε_1^{xx} $(\omega \rightarrow 0)$ component is larger than the $\varepsilon_1^{zz}(\omega \rightarrow 0)$ component. The $\varepsilon_1(0)$ value increases when the energy gap E_g decreases. This is in accordance with the Penn model[55]: $\varepsilon_1(0) \approx 1 + (\hbar\omega_p/E_g)^2$; $\varepsilon_1(0)$ is inversely proportional with E_g, i.e., smaller E_g yields larger $\varepsilon_1(0)$.

Figure 9 presents the frequency-dependent coefficient of absorption $\alpha(\omega)$, index of refraction $n(\omega)$, coefficient of extinction $k(\omega)$, reflectivity $R(\omega)$ and electron energy-loss function $L(\omega)$ for incident radiation polarized both along the a-axis ($\vec{E}//\vec{a}$) and c-axis ($\vec{E}//\vec{c}$) in a wider spectral region up to 30 eV. The optical spectra for $\vec{E}//\vec{a}$ are quite different from those for $\vec{E}//\vec{c}$, implying the optical anisotropy of these systems. The optical absorption coefficient $\alpha(\omega)$ is an important criterion to judge if a material could have an eventual application in the photoelectric field. The examined compounds exhibit a high coefficient of absorption (higher than 10^4 cm^{-1}) in a large energy range extending from the absorption edge E_g (from ~2.6 eV to 2.9 eV) up to 30 eV, suggesting that they could be suitable absorber layers for photovoltaic applications. Obviously, these materials with a band gap higher than 2.6 eV may absorb the blue and violet rays of the visible spectrum. The calculated refractive index spectra for the three examined materials are given in Fig. 9b. The refractive index reaches its maximum in the near ultraviolet (~3.8–5 eV). One can note the refractive index value increases when going from BaAgSF to BaAgSeF to BaAgTeF, which is in accordance with the usual trend of the refractive index, i.e., the refractive index increases when the band gap decreases. The calculated static refractive index ($n(0)$), which is a very important physical quantity for semiconductors, is listed in Table XII. From Fig. 9d, one can observe that the title systems exhibit a weak reflectivity at low energies and the magnitude of the reflectivity increases slightly when going from BaAgSF to BaAgSeF to BaAgTeF. Calculated static reflectivity coefficients ($R(0)$) of the three studied systems are given in Table XII. The energy loss-function $L(\omega)$ spectra are depicted in Fig. 9e.

CONCLUSIONS

Structural, elastic, electronic and optical properties of three LaOAgS-type silver fluoride chalcogenides: BaAgSF, BaAgSeF and BaAgTeF were studied in the present work using first-principles density theory calculations. Successful determination of the equilibrium structural parameters of the BaAg*Ch*F materials using pseudopotential plane-wave density functional theory reveals that an increase of the atomic number of the *Ch* chalcogenide element leads to an increase of the lattice constants and a decrease of the bulk modulus. The *a*-axis is more resistant to compressional deformations than the *c*-axis. After that, single-crystal and polycrystalline elastic moduli and related properties were numerically estimated. The obtained results reveal that the considered materials can be classified as soft materials with ductile character and a considerable elastic anisotropy.

DFT-based FP-LAPW method within the GGA08 and TB-mBJ functionals was used to perform the band structure and density of states diagrams. The examined materials are found to be wide direct band gap Γ–Γ semiconductors, from ~2.6 eV to ~2.9 eV. An increase of the atomic number *Z* of the chalcogen element causes a decrease of the band gap value. The bottommost of the conduction band is contributed mainly by n*p*-*Ch*, 4*p*-Ag and 5*d*-Ba states. The topmost valence band is almost dispersionless and is contributed by the hybridized n*p*-*Ch* and 4*d*-Ag states. The inter-atomic chemical bonding inside the [Ag*Ch*] blocks is of covalent character while that inside the [BaF] ones is of ionic character. Based on the accurate band structure obtained using TB-mBJ, the absorptive and dispersive parts of the dielectric function, absorption coefficient, refractive index, extinction coefficient, optical reflectivity and energy-loss function spectra were calculated for the [100] and [001] polarized incident radiation in a wide energy range up to 30 eV. The calculated optical spectra show a noticeable anisotropy. An increase of the atomic number of the *Ch* element leads to an increase of the magnitude of the peaks of the optical spectra. The zero-frequency limit $\varepsilon_1(0)$ increases when the energy band gap value decreases. The origins of the observed structures in the optical spectra are assigned in terms of the calculated energy band structure.

ACKNOWLEDGEMENT

The authors (A. Bouhemadou and S. Bin-Omran) extend their appreciation to the International Scientific Partnership Program ISPP at King Saud University for funding this research work through JSPP# 0025.

REFERENCES

1. D.O. Charkin, P.S. Berdonosov, V.A. Dolgikh, and P. Lightfoot, *J. Alloys Compd.* 292, 118 (1999).
2. D.O. Charkin, A.V. Urmanov, and S.M. Kazakov, *J. Alloys Compd.* 516, 134 (2012).
3. D.O. Charkin, A.V. Urmanov, I.V. Plokhikh, A.D. Korshunov, A.N. Kuznetsov, and S.M. Kazakov, *J. Alloys Compd.* 585, 644 (2014).
4. D.O. Charkin and X.N. Zolotova, *Crystallogr. Rev.* 13, 201 (2007).
5. A. Zakutayev, R. Kykyneshi, G. Schneider, D.H. McIntyre, and J. Tate, *Phys. Rev. B* 81, 155103 (2010).
6. V.K. Gudelli, V. Kanchana, G. Vaitheeswaran, D.J. Singh, A. Svane, N.E. Christensen, and S.D. Mahanti, *Phys. Rev. B* 92, 045206 (2015).
7. R. Pöttgen and D. Johrendt, *Z. Naturforsch. B* 63, 1135 (2008).
8. M. Palazzi and S. Jaulmes, *Acta Cryst. B* 37, 1337 (1981).
9. K. Ueda, H. Hiramatsu, M. Hirano, T. Kamiya, M. Hirano, and H. Hosono, *Thin Solid Films* 496, 8 (2006).
10. H. Yanagi, S. Ohno, T. Kamiya, H. Hiramatsu, M. Hirano, and H. Hosono, *J. Appl. Phys.* 100, 033717 (2006).
11. Y. Kamihara, T. Watanabe, M. Hirano, and H. Hosono, *J. Am. Chem. Soc.* 130, 3296 (2008).
12. V.V. Bannikov, I.R. Shein, and A.L. Ivanovskii, *J. Solid State Chem.* 196, 601 (2012).
13. J.F. Wager, D.A. Keszler, and R.E. Presley, *Transparent Electronics* (Berlin: Springer, 2008).
14. M. Yasukawa, K. Ueda, and H. Hosono, *J. Appl. Phys.* 95, 3594 (2004).
15. H. Hiramatsu, K. Ueda, H. Ohta, T. Kamiya, and M. Hirano, *Appl. Phys. Lett.* 87, 211107 (2005).
16. J.A. Spies, R. Schafer, J.F. Wager, P. Hersh, H.A.S. Platt, D.A. Keszler, G. Schneider, R. Kykyneshi, J. Tate, X. Liu, A.D. Compaan, and W.N. Shafarman, *Sol. Energy Mater. Sol. Cells* 93, 1296 (2009).
17. D.C. Johnston, *Adv. Phys.* 59, 803 (2010).
18. K. Ueda, H. Hiramatsu, H. Ohta, M. Hirano, T. Kamiya, and H. Hosono, *Phys. Rev. B* 69, 55305 (2004).
19. H. Kamioka, H. Hiramatsu, M. Hirano, K. Ueda, T. Kamiya, and H. Hosono, *J. Lumin.* 112, 66 (2005).
20. V.V. Bannikov, I.R. Shein, and A.L. Ivanovskii, *Solid State Commun.* 150, 2069 (2010).
21. V.V. Bannikov, I.R. Shein, and A.L. Ivanovskii, *Solid State Sci.* 14, 89 (2012).
22. J.P. Perdew, S. Burke, and M. Ernzerhof, *Phys. Rev. Lett.* 77, 3865 (1996).
23. C.S. Wang and W.T. Pickett, *Phys. Rev. Lett.* 7, 597 (1983).
24. W.G. Aulbur, L. Jönsson, and J.W. Wilkins, *Solid State Phys.* 54, 1 (1999).
25. S.Zh. Karazhanov, P. Ravindran, H. Fjellvag, and B.G. Svensson, *J. Appl. Phys.* 106, 123701 (2009).
26. O. Boudrifa, A. Bouhemadou, Ş. Uğur, R. Khenata, S. Bin-Omran, and Y. Al-Douri, *Philos. Mag.* 96, 2328 (2016).
27. A. Bouhemadou, D. Allali, S. Bin-Omran, E.M.A. Al Safi, R. Khenata, and Y. Al-Douri, *Mater. Sci. Semicond. Process.* 38, 192 (2015).
28. S.J. Clark, M.D. Segall, C.J. Pickard, P.J. Hasnip, M.J. Probert, K. Refson, and M.C. Payne, *Z. fuer Kristallographie* 220, 567 (2005).
29. J.P. Perdew and A. Zunger, *Phys. Rev. B* 23, 5048 (1981).
30. J.P. Perdew, A. Ruzsinszky, G.I. Csonka, O.A. Vydrov, G.E. Scuseria, L.A. Constantin, X. Zhou, and K. Burke, *Phys. Rev. Lett.* 100, 136406 (2008).
31. D. Vanderbilt, *Phys. Rev. B* 41, 7892 (1990).
32. J.D. Pack and H.J. Monkhorst, *Phys. Rev. B* 16, 1748 (1977).
33. T.H. Fischer and J. Almlof, *J. Phys. Chem.* 96, 9768 (1992).
34. H. Hill, *Phys. Soc. Sect. A Proc.* 65, 349 (1952).
35. A.D. Becke and E.R. Johnson, *J. Chem. Phys.* 124, 221101 (2006).
36. F. Tran, P. Blaha, and K. Schwarz, *J. Phys. Condens. Matter* 19, 196208 (2007).
37. F. Tran and P. Blaha, *Phys. Rev. Lett.* 102, 226401 (2009).
38. D. Koller, F. Tran, and P. Blaha, *Phys. Rev. B* 83, 195134 (2001).
39. P. Blaha, K. Schwarz, G.K.H. Madsen, D. Kvasnicka, and J. Luitz, *An Augmented Plane Wave + Local Orbitals Program for Calculating Crystal Properties* (Wien: University Karlheinz Schwarz, 2013).

40. F. Birch, *Phys. Rev.* 71, 809 (1947).
41. F.D. Murnaghan, *Natl. Acad. Sci. Proc.* 30, 244 (1944).
42. P. Vinet, J.H. Rose, J. Ferrante, and J.R. Smith, *J. Phys. Condens. Matter* 1, 1941 (1989).
43. M. Born and K. Huang, *Dynamical Theory of Crystal Lattices* (Oxford: Clarendon Press, 1965).
44. Z.J. Wu, E.J. Zhao, H.P. Xiang, X.F. Fao, X.J. Liu, and J. Meng, *Phys. Rev. B* 76, 054115 (2007).
45. S.F. Pugh, *Philos. Mag.* 45, 823 (1954).
46. P. Ravindran, L. Fast, P.A. Korzhavyi, B. Johansson, J. Wills, and O. Eriksson, *J. Appl. Phys.* 84, 4891 (1998).
47. P. Lloveras, T. Castán, M. Porta, A. Planes, and A. Saxena, *Phys. Rev. Lett.* 100, 165707 (2008).
48. S.I. Ranganathan and M. Ostoja-Starzewski, *Phys. Rev. Lett.* 101, 055504 (2008).
49. J.F. Nye, *Properties of Crystals* (Oxford: Clarendon Press, 1985).
50. A. Bedjaoui, A. Bouhemadou, and S. Bin-Omran, *High Press. Res.* 36, 198 (2016).
51. O.L. Anderson, *J. Phys. Chem. Solids* 24, 909 (1963).
52. E. Schreiber, O.L. Anderson, and N. Soga, *Elastic Constants and Their Measurements* (New York: McGraw-Hill, 1973).
53. J. Feng, B. Xiao, R. Zhou, W. Pan, and D.R. Clarke, *Acta Mater.* 60, 3380 (2012).
54. H. Yanagi, J. Tate, S. Park, C.H. Park, D.A. Keszler, M. Hirano, and H. Hosono, *J. Appl. Phys.* 100, 083705 (2006).
55. D.R. Penn, *Phys. Rev.* 128, 2093 (1960).